Published in final edited form as:
Magn Reson Med. 2012 December ; 68(6): 1764–1773. doi:10.1002/mrm.24520.

Natural D-Glucose as a biodegradable MRI contrast agent for detecting cancer

Kannie W. Y. Chan[1,2], **Michael T. McMahon**[1,3,*], **Yoshinori Kato**[4,5,6], **Guanshu Liu**[1,3], **Jeff W.M. Bulte**[1,2], **Zaver M. Bhujwalla**[4,5,6], **Dmitri Artemov**[4,5,6], and **Peter C. M. van Zijl**[1,3,6,*]

[1]Russell H. Morgan Department of Radiology and Radiological Science, Division of MR Research, The Johns Hopkins University School of Medicine, Baltimore, Maryland, USA

[2]Cellular Imaging Section and Vascular Biology Program, Institute for Cell Engineering, The Johns Hopkins University School of Medicine, Baltimore, Maryland, USA

[3]F.M. Kirby Research Center for Functional Brain Imaging, Kennedy Krieger Institute, Baltimore, Maryland, USA

[4]Division of Cancer Imaging Research, The Johns Hopkins University School of Medicine, Baltimore, Maryland, USA

[5]JHU In vivo Cellular Molecular Imaging Center, The Johns Hopkins University School of Medicine, Baltimore, Maryland, USA

[6]Department of Oncology, The Sidney Kimmel Comprehensive Cancer Center at Johns Hopkins, Baltimore, Maryland, USA

Abstract

Purpose—Modern imaging technologies such as CT, PET, SPECT, and MRI employ contrast agents to visualize the tumor microenvironment, providing information on malignancy and response to treatment. Currently, all clinical imaging agents require chemical labeling, i.e. with iodine (CT), radioisotopes (PET/SPECT), or paramagnetic metals (MRI). The goal was to explore the possibility of using simple D-glucose as an infusable biodegradable MRI agent for cancer detection.

Methods—D-glucose signals were detected using chemical exchange saturation transfer (glucoCEST) MRI of its hydroxyl groups. Feasibility was established in phantoms as well as in vivo using two human breast cancer cell lines, MDA-MB-231 and MCF-7, implanted orthotopically in nude mice. PET and contrast-enhanced MRI were also acquired.

Results—Both tumor types exhibited significant glucoCEST signal enhancement during systemic sugar infusion (mild hyperglycemia), allowing their noninvasive visualization. GlucoCEST showed differences between types, while PET and CE-MRI did not. Data are discussed in terms of signal contributions from the increased vascular volume in tumors and especially from the acidic extracellular extravascular space (EES), where glucoCEST signal is expected to be enhanced due to a slow-down of hydroxyl proton exchange.

Conclusions—This observation opens up the possibility for using simple non-toxic sugars as contrast agents for cancer detection with MRI by employing hydroxyl protons as a natural label.

Keywords

glucose; MRI; cancer detection; screening; contrast agent; biodegradable

*To whom correspondence may be addressed. pvanzijl@mri.jhu.edu; mcmahon@mri.jhu.edu.

Introduction

Cancer remains one of the leading causes of death in the industrialized world, and continuous development of noninvasive imaging methods is needed to improve diagnosis and especially prognosis. For better therapeutic outcomes, it is essential to identify and determine different stages of tumor development, the likelihood of metastasis, and the presence of recurrent tumor versus treatment necrosis. Solid tumors such as gliomas and prostate and breast carcinomas have several evolutionary characteristics that reveal their aggressiveness. These include aerobic glycolysis (1) and a concomitant increase in lactate production (1–7), an acidic extravascular and extracellular space (EES) consequential to lactate efflux from cells with normal pH, an enlarged leaky vasculature due to angiogenesis, and an upregulation of the glucose transporters GLUT1 and GLUT3 (8,9).

To improve cancer prognosis, imaging technologies are being designed that can detect these physiological features (7,10). For instance, increases in glucose uptake can be imaged by ^{18}FDG-PET, while lactate metabolism can be studied using hyperpolarized ^{13}C pyruvate imaging (11). Changes in perfusion properties such as vascular volume, volume of EES and vascular permeability can be assessed by dynamic contrast enhanced (DCE) MRI or computed tomography (CT) and, more recently, arterial spin labeling (12) which requires no contrast injection. Currently, all clinical agents for the three leading methodologies require some form of chemical labeling, i.e. with iodine (CT), radioisotopes (PET), or paramagnetic metals (MRI). We here propose a paradigm shift by developing the use of a biodegradable agent, namely simple D-glucose that has a natural MRI label. We detect this compound using the emerging MRI contrast mechanism of “chemical exchange saturation transfer” or “CEST” (13–15), which can sense the presence of low concentrations of exchangeable protons (mM range) with molar sensitivity via the water signal used in MRI. In the preclinical setting, CEST imaging has been performed using exogenous paramagnetic (15–18) and diamagnetic agents (14,19,20), while endogenous compounds (21–24) have been detected in situ in humans. We recently showed (23) that CEST can detect the presence of hydroxyl protons on glycogen (glycoCEST) and D-glucose (glucoCEST).

The suitability of D-glucose as an MRI contrast agent to detect cancer at first seems unlikely, because glucose taken up by tumors is rapidly metabolized to lactate and the intracellular concentrations of D-glucose and intermediate sugars in the breakdown pathway are negligible (1–6). However, we hypothesized that the large extracellular volume fraction in tumors (30–40%) (2,25,26), dominated by the acidic interstitial space (EES) (27–29), should provide favorable conditions for CEST detection of rapidly exchanging OH protons because it will slow down such exchange for increased detection sensitivity. We here demonstrate the possibility to image glucose uptake in two human breast cancer cell lines, MDA-MB-231 and MCF-7, implanted orthotopically in nude mice and compare this uptake with ^{18}FDG-PET and Gd-DTPA contrast. The results indicate that glucoCEST detection of changes in glucose concentration during infusion readily visualizes the tumors and provides information about the tumor microenvironment complementary to that of ^{18}FDG-PET and Gd-enhanced MRI studies. While uptake in PET reflects glucose metabolism and uptake in dynamic Gd studies reflects perfusion and vascular permeability for GdDTPA, uptake in glucoCEST difference imaging reflects the equilibrium between perfusion, vascular and cellular permeability for glucose, and tumor metabolism as visualized mainly through increased visibility of glucose hydroxyl groups in EES. A preliminary account of this work has appeared in abstract form by our group in 2011 (30). At the same time, Golay et al. showed the use of glucoCEST to detect fluorodeoxyglucose (31) followed by 2012 reports of the application of D-glucose (32,33).

Methods

Phantom preparation

D-glucose (Sigma-Aldrich) was dissolved in phosphate buffered saline (PBS at pH 7.3, 6.2 or 6.8) at concentrations of 10, 20, 50, 100 and 200 mM. To ascertain correct concentrations, the pH was titrated to the required value before dilution to 20 mM.

Implantation of human cancer cells in mice

Experiments were performed in accordance with Institutional Animal Care and Use Committee guidelines. Female athymic nude mice (*nu/nu*; National Cancer Institute, MD) were inoculated with both MDA-MB-231 and MCF-7 xenografts on contralateral sides. Mice were anesthetized with intraperitoneal injections of a mixture of ketamine and xylazine (0.15 ml; 62.5 mg/kg and 6.25 mg/kg, respectively). MDA-MB-231 (1×10^6 cells) and MCF-7 cells (3×10^6 cells) in 0.05 ml of Hanks balanced salt solution were implanted orthotopically into the upper thoracic mammary fat pad. MDA-MB-231 cells were injected into the upper right, and MCF-7 cells into the upper left. An estrogen pellet (17β-estradiol, Innovative Research of America, Inc.) was implanted with a sterilized 10G trocar needle in the lateral side of the neck of the animal 24–48 hours prior to the MCF-7 cell inoculation, and the opening was closed with a single sterile suture clip. The total dose was 0.18 mg/pellet released over 60 days. Tumor sizes were checked after 6 and 12 h, and then daily. MDA-MB-231 tumors were inoculated 18 days before imaging and slower growing MCF-7 tumors 1 month before. Imaged mice had average tumor size ranging from 3×5 mm^2 to 3×6 mm^2.

Infusion protocols

Female athymic nude mice bearing both MDA-MB-231 and MCF-7 tumors were fasted overnight with water access before imaging. Mice were anesthetized by isoflurane, and kept warm with a heating bed. The tail vein was cannulated for administration of glucose or Gd-DTPA. A home-built catheter was connected to a syringe pump for glucose infusion through a line with the dead volume minimized to 40 μL. We used PE-60 tubing (Becton Dickinson) and two T-connectors (1/16”, Cole-Parmer) to assemble a connector with 4 outlets, which were connected to the glucose solution (0.5 M in saline), Gd-DTPA solution (Magnevist®; 100 mM in saline), heparinized saline and the tail vein of the mouse respectively. A 25G needle was used to connect the PE-60 tubing to the syringes. A 3 ml syringe with 0.5 M glucose solution was positioned at a syringe pump for infusion, and 1 ml syringes were used for saline and Gd-DTPA injection. Except the line connected to the tail vein, all lines were controlled by two-way stopcocks, and only one line was open at any time. The line containing saline was used to test the potency of the tail vein.

D-glucose (0.5 M in saline) was infused via the tail vein at an initial rate of 1.5 ml/h for a period of 5 min, followed by 0.9 ml/h for 10 min and 0.12 ml/h for 15 min (Fig. 1a, black line). To test the blood glucose concentration upon infusion, we first performed experiments outside the magnet in which D-glucose was infused in non-tumor bearing mice. The blood glucose concentration was measured at 0, 5, 15, 30, 45 and 60 min (Fig. 1a, red line). For two mice, the average blood glucose concentrations were 5.2 ± 1.2 mM and 14.7 ± 0.9 mM before and during infusion.

Gd-DTPA was administered via the same tail vein after the glucoCEST measurements (n=5; 0.5 mmol/kg; 0.1 ml bolus i.v. over about 3 s).

Imaging

Our experimental imaging protocol is summarized in Fig. 1b. Five mice carrying both tumors underwent PET and glucoCEST and contrast-enhanced MRI. After an initial PET study one day before MRI and overnight fasting, we performed two 25 min glucoCEST acquisitions, one before infusion and one during infusion when the glucose level in blood was constant at about 12–15 mM (Fig. 1a). After stopping the glucose infusion and following an additional minimal waiting period of 30 min after completing the glucoCEST acquisition, contrast-enhanced MRI was performed.

PET acquisition—Uptake of ^{18}FDG was imaged with the eXplore Vista small animal PET scanner 1 hour after i.v. injection of ^{18}FDG (200 μCi). Then, the animal still fixed on the cradle was imaged at the Gamma Medica X-SPECT scanner where a CT image of the whole body was acquired to identify the location of the tumors.

CEST MRI acquisition—All MRI images were acquired on a 11.7T Bruker Biospec system equipped with a 23 mm transceiver coil. After manual shimming, two sets of saturation images were collected: a WAter Saturation Shift Reference (WASSR, (34)) set for B_0 mapping and a CEST Z-spectrum. Both were acquired using a modified Rapid Acquisition with Relaxation Enhancement (RARE) sequence containing a single continuous wave magnetization transfer (MT) prepulse. The acquisition parameters for 5 mm phantoms were: TR = 1.5 s for WASSR and 6.0 s for CEST, effective TE = 4.7 ms, RARE factor = 16, slice thickness 1 mm, acquisition matrix 128×64, field of view of 23×20 mm^2, 2 averages. The saturation offset range was ±1 ppm (0.1 ppm steps) with respect to water in WASSR spectra and ±4 ppm (0.2 ppm steps) in Z-spectra. For WASSR, the saturation parameters were t_{sat} = 500 ms and B_1 = 0.5 μT. For the phantom Z-spectra saturation parameters were t_{sat} = 4s, and B_1 = 1.6, 2.0, 2.4, 3.0 and 3.6 μT. All studies were carried out at 37 °C.

In vivo axial images were acquired with the imaging scheme described above except for addition of a fat suppression pulse (3.4 ms hermite pulse, offset = −3.5 ppm). The acquisition parameters for the glucoCEST Z-spectrum were: TR =5.0 s, effective TE = 5 ms, RARE factor = 12, t_{sat} = 4s, B_1 = 1.6 μT, slice thickness = 1 mm, acquisition matrix size 96×48, FOV of 21×20 mm^2, and two averages. For the CEST contrast measurements at steady state the Z-spectral offset range was ±4 ppm with ±0.2 ppm steps, collected over 25 min.

CE-MRI acquisition—Multislice T_1 mapping was performed for a slice envelope that included the same slice as the CEST imaging with matrix size 128×80 and a slice thickness of 1 mm. A nonselective saturation recovery gradient echo sequence with TE/TR=1.45/30ms, and flip angle 90° was used to suppress effects of water exchange on the measured signal enhancement (35). Briefly, this sequence employed nonselective saturation of magnetization by a composite RF pulse followed by a variable crusher gradient and a 25 ms recovery period, which was repeated for all phase encoding steps and slices. The total acquisition time for 5 slices was approximately 12 sec. After a series of 8 pre-contrast images, Gd-DTPA was injected and 24 post-contrast images were collected over about 5 min.

CEST MRI data processing and statistics

All data were processed using custom-written scripts in MATLAB (Mathworks, Waltham, MA). Regions of interest (ROIs) were drawn manually based on the T_2-weighted images. Mean Z-spectra, which display the ratio of the MRI water signal intensity during RF saturation (S) and without saturation (S_0) as a function of saturation frequency offset ($\Delta\omega$) with respect to water, were calculated after B_0 correction on a per voxel basis using

WASSR. GlucoCEST contrast was quantified over the offset range 0.8 – 2.2 ppm using a magnetization transfer ratio (MTR) asymmetry analysis with respect to the water frequency:

$$MTR_{asym}(\Delta\omega)=S(-\Delta\omega)/S_0 - S(\Delta\omega)/S_0$$

For the *in vivo* analysis, ROIs were drawn manually on MCF-7 and MDA-MB-231 tumors based on the T_2-weighted images. The mean intensities were used for MTR_{asym}, and ΔMTR_{asym} was calculated by subtracting the mean MTR_{asym} pre-infusion from that during infusion.

Student's paired t-tests were used for statistical testing, and were considered significant when $p<0.05$.

Results

Phantom studies of D-glucose

In order to show that D-glucose can be detected in millimolar concentrations under physiological conditions and that detection should be enhanced in EES, we first studied saturation spectra in a series of phantoms at different pH and different B_1. The Z-spectra (Figures 2a,b top) show that the presence of D-glucose causes an asymmetry of the S/S_0 curve towards higher frequency, leading to a robust MTR_{asym} between 0.5 and 2.2 ppm at pH = 7.3 (bottom of Figs. 2a,b). Increasing the glucose concentration causes a broadening of the line shape of the direct water saturation and an apparent shift of the maximum of the MTR_{asym} curve to higher frequency. Therefore, to assure minimal influence of the direct saturation broadening, we analyze the averaged signal intensity from 0.8 to 2.2 ppm. When doing this, a glucoCEST effect of about 0.31 % per mM is visible for a B_1 of 1.6 μT, which corresponds to about 0.34 M water signal or a signal enhancement by a factor of 340.

The MTR_{asym} line shape at pH = 7.3 is asymmetric and featureless, which changes when acidifying the solution (Fig. 2b). Several resonances become visible at lower pH, corresponding to five OH groups in D-glucose with different chemical shifts, as assigned previously at low pH and low temperature in H_2O (36). Notice that the intensities of these groups do not need to be proportional because they depend on the exchange rate for each individual OH. Interestingly, in the MTR_{asym} spectra, there is a shift of the maximum effect from 0.8 to about 1.2–1.3 ppm, which should benefit *in vivo* detection as it is further away from the water frequency. These features do not change appreciably when irradiating the samples with higher saturation fields (Fig. 2c), but sensitivity increases strongly because higher B_1 facilitates the detection of rapidly exchanging protons such as OH groups. The reason is that more saturation can be induced before exchange occurs. However, the direct saturation water line broadens with B_1 and will compete with the glucoCEST effect. *In vivo*, T_2 is shorter, broadening the direct saturation even more. In addition, the contribution of conventional MT effects increases with B_1. We therefore decided to use a B_1 of 1.6 μT *in vivo*.

The glucoCEST contrast is linear at low concentration (23) but becomes non-linear at higher concentrations (Fig. 2d), which is a well-known CEST phenomenon reflecting back-exchange of saturated protons (19,37,38). For high exchange rates and multiple sites, this concentration dependence cannot be described by the analytical CEST solution anymore (19,37,38) and needs to be fitted using the Bloch equations. To obtain an estimated exchange rate, we fitted the data assuming one combined OH resonance for 3 protons at 1.3 ppm, giving an OH exchange rate of ~2.3 kHz at pH 7.3 (using QUESP (38)), and ~1.1 kHz at pH 6.8 and 6.2. In order to estimate the possible *in vivo* effects for a combined broad

glucose signal, one can use the averaged glucoCEST signal intensities over the range from 0.8–2.2 ppm from the 20 mM solution. These were 6.2%, 9.7% and 8.3% for pH = 7,3, 6.8 and 6.2, respectively. In our *in vivo* infusion protocol, the plasma glucose concentration is ramped up to approximately 15 mM (Fig. 1a). For a typical tumor vascular volume fraction of about 0.05 – 0.08 (2,39), the integrated vascular glucoCEST signal would be about 15×0.31% times that fraction (0.23 – 0.37 %). Using an EES volume of about 0.35 (25), the EES glucoCEST contribution per mM glucose would be 0.109%, 0.170% and 0.145% at pH = 7.3, 6.8 and 6.2, respectively. Assuming unrestricted glucose transport (15 mM) into the EES and a vascular fraction of 0.05, the glucoCEST effect can be estimated to be 1.9%, 2.8% and 2.4% for these three pH values. These phantom data indicate that *in vivo* imaging should be feasible with an effect around 2–3%.

In vivo breast tumor studies

GlucoCEST was tested on two well-known human breast cancer xenograft models, highly malignant triple negative (estrogen receptor/progesterone receptor /Her-2 neu) MDA-MB-231 tumors and less aggressive (estrogen receptor positive) MCF-7 tumors, orthotopically implanted in female athymic *nu/nu* mice at different time points to allow approximately comparable tumor size (Fig. 3a). Figs. 3b and 3c show pre-infusion and infusion glucoCEST MTR_{asym} images respectively for the averaged 0.8–2.2 ppm spectral region. These individual MTR_{asym} images show contrast in both muscle and tumor, but are complicated to interpret because they contain multiple endogenous saturation transfer effects (23,40). This is clear in the MTR_{asym} spectra for the MDA-MB-231 and MCF-7 tumors (Figs. 3d,e, respectively), which show a frequency dependence with positive and negative components similar to those found in brain tumors (40) and explained previously in terms of an inherent asymmetry in the conventional MT effect for semi-solid tissue components such as membranes. Such effects make the baseline MTR_{asym} spectra almost impossible to interpret in terms of glucose contributions. However, when analyzing the tumor regions, a significant difference is found between before and during infusion among five animals (Fig. 3f). We therefore generated an infusion/pre-infusion difference image (ΔMTR_{asym}, Fig. 3g) in which the endogenous contributions are expected to drop out. When doing so, we found that the central part of the body contained many artifacts in such low-SNR difference images and thresholded it out. Interestingly, the spectral profiles for the tumor regions in the, ΔMTR_{asym} maps (Fig. 3h) show a profile with positive intensities resembling the D-glucose MTR_{asym} data in the phantoms (Fig. 2). The presence of observable intensities in the 2–3 ppm range suggests that the spectra are representative of regions with lower pH. The average ΔMTR_{asym} spectra in Fig. 3i show good reproducibility among mice leading to statistically significant increases in MTR_{asym} upon infusion in both tumors (Fig. 3f).

Fig. 4 summarizes PET, glucoCEST and Gd-based contrast-enhanced (CE) MRI results for five animals. All three modalities show signal changes outside the tumors too. For glucoCEST difference images these could possibly be due to the presence of blood vessels (blood glucose concentration was 12–15 mM) and small motion artifacts in the difference images that are enhanced by low SNR. All modalities showed significant signal increases (n = 5) in tumor tissue upon administration of each of the contrast agents, allowing detection of these malignancies. In PET, signals were compared to background (both tumors: $p<0.01$), while for MRI the signals pre-infusion and during infusion were used. Signals of both MDA-MB-231 and MCF-7 increased significantly for CE-MRI ($p<0.05$ and $p<0.01$ respectively) and glucoCEST, ($p<0.05$ and $p<0.005$, respectively).

Interestingly, when comparing tumor types for the three modalities, the data were less informative (Figs. 4d–f). Despite the visibility of a trend that PET uptake is larger for MDA-MB-231 versus MCF-7 (Fig. 4d), neither PET nor CE-MRI (Fig. 4f) could significantly

distinguish the two tumors. In glucoCEST, on the other hand, a significant difference between tumors was evident ($p<0.05$; paired t-test; Figs. 4e,g).

When studying the images, the PET and glucoCEST data showed a reasonably homogeneous uptake throughout the tumor, while CE-MRI showed uptake only in limited regions. In an effort to see whether glucoCEST data differed between regions with and without Gd uptake, we also assessed a smaller ROI prescribed only in regions of contrast enhancement (Fig. 5). Again a characteristic glucose profile was visible in the ΔMTR_{asym} spectra (Fig. 5a), together with significantly lower glucoCEST contrast in MDA-MB-231 tumors compared to MCF-7 (Fig. 5b, $p<0.05$; paired t-test). This was not the case for Gd-enhanced MRI (Fig. 5c, $p>0.05$; paired t-test).

Discussion

Except for some of the small molecules used in PET and ^{13}C NMR, contrast agents generally are not biodegradable. Our data show that it is possible to use one of the body's building blocks, the simple carbohydrate D-glucose, and the interaction of its hydroxyl protons with the body's own solvent, water, to detect tumors. GlucoCEST difference images (Fig. 3g) showed significant signal enhancement in the tumor regions, the viability of which was validated with FDG-PET and CE-MRI. However, it is important to point out that the spatial origin of these three types of contrast in the tumor microenvironment is different and to a great deal complimentary. For instance, the accumulation of intracellular phosphorylated deoxyglucose in ^{18}FDG-PET reflects tumor metabolism, the rate-determining step of which is known to be glucose transport (1–4,41,42). Contrast-enhanced MRI reflects the permeability of the tumor vasculature for the agent Gd-DTPA, which is lower than for FDG and D-glucose, which freely enter the interstitium in most tissues except the brain (43). In line with these expectations, the data indeed showed that FDG and D-glucose were readily taken up throughout the tumor, while only partial Gd-enhancement was visible. The glucoCEST difference images provided significant contrast with surrounding muscle. Based on well-established knowledge regarding metabolism of solid tumors (4) it is unlikely that any intracellular D-glucose or phosphorylated glucose derivatives contribute to glucoCEST because these have been shown to be metabolized rapidly to lactate (1–4,42,44). In addition to a small vascular contribution, we therefore attribute the glucoCEST mostly to signal from EES, the size of which is increased in tumors and known to be acidic compared to intracellular space. To compare the underlying mechanisms for these contrasts, the expected pathways of uptake for the different modalities are summarized in Fig. 6, with color intensities depicting the contribution to the signal.

For the current two tumor types, only glucoCEST provided significant contrast between the MDA-MB-231 and MCF-7 tumors, while PET and CE-MRI did not. For ^{18}FDG-PET, this result is in exact agreement with a recent study by McLarty et al (45) on these two tumor types in CD1 *nu/nu* mice. For CE-MRI we could not find a comparative study between MCF-7 and MDA-MB-231. Interestingly, the glucoCEST signal was consistently lower in MDA-MB-231 for all animals (Fig. 4e), confirming our expectation that glucoCEST is not particularly representative of glucose metabolism. MDA-MB-231 cells are expected to be more acidic (27,46,47) with respect to MCF-7, but because the integral of the glucose signal peaks at pH = 6.8 (for the pH points measured), it could well be that the MCF-7 signal is higher due to optimal EES exchange conditions compared to MDA-MB-231. Possible alternative explanations are that the MCF-7 tumors have lower cellularity and thus a larger EES or that the EES of MDA-MB-231 has a reduced glucose concentration as a consequence of higher glucose metabolism of these more malignant cells (1,42). Thus more experiments are needed to better understand these initial results and one confound of the current experiments is that they will be affected by heterogenous glucose uptake and pH

distribution. However, tumors are known to be heterogeneous and other methods such as PET and CE-MRI typically suffer from similar limitations. With respect to this, it is important to realize that while many OH or NH_2 containing compounds can contribute to the glucoCEST spectrum around 1ppm (for instance glycogen (48)), it is unlikely that these contribute significantly to the glucoCEST difference image unless a metabolic product based on glucose as a substrate is formed or the pH in the compartments of interest is adjusted due to the increased glucose concentration.

The glucoCEST signal in the two tumors for the individual animals ranged from 1–4% (Fig. 4e), in line with estimates made from our phantom studies based on the size of the EES previously reported by others in CE-MRI studies (2,25,26). This and the contrast with muscle supports our hypothesis that the acidic pH in the interstitium (27) aids the *in vivo* visualization of glucose in tumors. Thus, we conclude that the glucoCEST contrast in its current form does not directly provide information on metabolism but mainly on EES. In principle, therefore, it is not necessary to use glucose as a contrast agent and any CEST agent that readily enters the EES and is sensitive to pH can be employed. If very pH-sensitive biodegradable contrast agents can be designed these could replace glucose in the future. However, this would require toxicology testing and approval by the regulating agencies (e.g. FDA in the USA), while glucose is already approved for other indications.

Of course the question arises whether D-glucose can be used to study metabolism. Although not part of the current study, we would like to speculate that glucoCEST can in principle provide information on tumor perfusion as well as metabolism because both are involved in its signal (Fig. 6). However, this would have to be done with high temporal resolution using an imaging scheme appropriate for dynamic data collection. For perfusion, this would require a bolus followed by imaging every few seconds, similar to Gd-DTPA, for which we did not have the sensitivity in the current study. As such, it would also be more complicated than ASL, which can be used without any contrast, and is recently becoming more accessible in the clinic, allowing the study of perfusion in brain tumors (12,49–54), breast cancer (55,56) and renal cell carcinoma (57). If glucose metabolism were to be studied, this could involve a rapid monitoring of the decay of the glucoCEST signal after stopping the infusion. Unlike normal tissue, tumors will rapidly clear glucose from EES because of their elevated glycolytic rates. We intend to explore this in the future. Such experiments should also provide some insight whether the difference in glucoCEST and GdDTPA. The occurrence of glucoCEST difference contrast throughout the tumor and at most partial enhancement of the tumor using Gd-DTPA seems to indicate a difference in vascular or tissue permeability for these two agents or could be due to a difference in administration approach (systemic hyperglycemia vs fast passage after bolus). However, it is unclear whether any differences in contrast appearance for the two approaches would exist if the tumors would have enhanced. Ultimately, the availability of PET-MRI may allow the simultaneous use of D-glucose and ^{18}FDG followed by Gd MRI for even more improved localization of tumor foci.

There are also some technical advantages that should facilitate clinical use of glucoCEST. First, contrary to most PET agents (which require synthesis close to the time of use) and hyperpolarized MRI (11) agents (which require hyperpolarization close to time of use), D-glucose is stable and already available as an injectable solution for human use. No additional equipment such as an on-site cyclotron, hyperpolarizer or ^{13}C RF coil is needed. Secondly, the CEST technology employs the proton nucleus and can thus be performed immediately on most clinical scanners (we expect fields of 1.5 Tesla and higher depending on the contrast agent). Third, D-glucose is expected to significantly reduce problems with adverse side affects in contrast studies, such as currently the case for iodinated CT agents and Gd-based contrast agents in patients with renal pathologies. One major advantage of D-glucose

is that it can be used at sufficiently high concentrations in vivo to allow MRI detection. For instance, in our experiments we used a 0.5 M solution to increase the plasma glucose concentration from baseline 4–5 mM to 12–15 mM. This is in the same blood concentration range as the glucose tolerance test commonly used in the clinic, where 50 ml of 50% D-glucose in water is injected (58), leading to blood glucose levels of 15–20 mM. We therefore expect translation of this new technology to the clinic to be readily feasible. As an alternative to intravenous glucose, it should be possible to perform oral administration. For instance, the amount of sugar in the i.v. glucose test corresponds approximately to that present in a soda beverage. Finally, the knowledge of drinking a sugary beverage or being injected with a natural sugar for an imaging study is expected to facilitate the peace of mind of the aware consumer when undergoing a scan with such contrast.

With respect to disadvantages, glucose tests may cause hypoglycemia and glucose may not be suitable for some populations, for instance patients with diabetes. So glucose monitoring may be needed. In addition, similar to magnetization transfer imaging, CEST-MRI has higher SAR than most sequences. However, we are routinely performing human CEST (APT) imaging on our 3T scanner (59–61) and we expect to be able to do this well within SAR limits for the glucose studies.

Conclusions

Annually, close to 40 million people worldwide are injected with a contrast agent for MRI, CT or PET. We demonstrated the feasibility of using D-glucose as a biodegradable contrast agent for MRI by exploiting its hydroxyl groups as a natural MRI chemical exchange label. We expect this will provide a low-risk alternative for patients with kidney disease and a complementary contrast for cancer studies in which PET and MRI are used for diagnosis and especially prognosis.

Acknowledgments

We thank Mr. Gilbert Green for his technical assistance in using the PET and CT scanners.

This work was supported by NIH grants P50CA103175 (NCI), R01EB015031, R01EB015032 (NIBIB) and S10RR028955 (NCRR).

References

1. Gatenby RA, Gillies RJ. Why do cancers have high aerobic glycolysis? Nat Rev Cancer. 2004; 4(11):891–899. [PubMed: 15516961]
2. Rivenzon-Segal D, Margalit R, Degani H. Glycolysis as a metabolic marker in orthotopic breast cancer, monitored by in vivo (13)C MRS. Am J Physiol. 2002; 283(4):E623–E630.
3. Rivenzon-Segal D, Rushkin E, Polak-Charcon S, Degani H. Glucose transporters and transport kinetics in retinoic acid-differentiated T47D human breast cancer cells. Am J Physiol. 2000; 279(3):E508–E519.
4. Artemov D, Bhujwalla ZM, Pilatus U, Glickson JD. Two-compartment model for determination of glycolytic rates of solid tumors by in vivo 13C NMR spectroscopy. NMR Biomed. 1998; 11(8): 395–404. [PubMed: 10221582]
5. Gottschalk S, Anderson N, Hainz C, Eckhardt SG, Serkova NJ. Imatinib (STI571)-mediated changes in glucose metabolism in human leukemia BCR-ABL-positive cells. Clin Cancer Res. 2004; 10(19):6661–6668. [PubMed: 15475456]
6. Kallinowski F, Vaupel P, Runkel S, Berg G, Fortmeyer HP, Baessler KH, Wagner K, Mueller-Klieser W, Walenta S. Glucose uptake, lactate release, ketone body turnover, metabolic micromilieu, and pH distributions in human breast cancer xenografts in nude rats. Cancer Res. 1988; 48(24 Pt 1):7264–7272. [PubMed: 3191497]

7. Brindle K. New approaches for imaging tumour responses to treatment. Nat Rev Cancer. 2008; 8(2): 94–107. [PubMed: 18202697]
8. Bos R, van Der Hoeven JJ, van Der Wall E, van Der Groep P, van Diest PJ, Comans EF, Joshi U, Semenza GL, Hoekstra OS, Lammertsma AA, Molthoff CF. Biologic correlates of (18)fluorodeoxyglucose uptake in human breast cancer measured by positron emission tomography. J Clin Oncol. 2002; 20(2):379–387. [PubMed: 11786564]
9. Krzeslak A, Wojcik-Krowiranda K, Forma E, Jozwiak P, Romanowicz H, Bienkiewicz A, Brys M. Expression of GLUT1 and GLUT3 glucose transporters in endometrial and breast cancers. Pathol Oncol Res. 2012; 18(3):721–728. [PubMed: 22270867]
10. Gambhir SS. Molecular imaging of cancer with positron emission tomography. Nat Rev Cancer. 2002; 2(9):683–693. [PubMed: 12209157]
11. Gallagher FA, Bohndiek SE, Kettunen MI, Lewis DY, Soloviev D, Brindle KM. Hyperpolarized 13C MRI and PET: in vivo tumor biochemistry. J Nucl Med. 2011; 52(9):1333–1336. [PubMed: 21849405]
12. Jarnum H, Steffensen EG, Knutsson L, Frund ET, Simonsen CW, Lundbye-Christensen S, Shankaranarayanan A, Alsop DC, Jensen FT, Larsson EM. Perfusion MRI of brain tumours: a comparative study of pseudo-continuous arterial spin labelling and dynamic susceptibility contrast imaging. Neuroradiology. 2010; 52(4):307–317. [PubMed: 19841916]
13. van Zijl PC, Yadav NN. Chemical exchange saturation transfer (CEST): what is in a name and what isn't? Magn Reson Med. 2011; 65(4):927–948. [PubMed: 21337419]
14. Ward KM, Aletras AH, Balaban RS. A new class of contrast agents for MRI based on proton chemical exchange dependent saturation transfer (CEST). J Magn Reson. 2000; 143(1):79–87. [PubMed: 10698648]
15. Ali MM, Liu GS, Shah T, Flask CA, Pagel MD. Using Two Chemical Exchange Saturation Transfer Magnetic Resonance Imaging Contrast Agents for Molecular Imaging Studies. Acc Chem Res. 2009; 42(7):915–924. [PubMed: 19514717]
16. Woods M, Woessner DE, Sherry AD. Paramagnetic lanthanide complexes as PARACEST agents for medical imaging. Chem Soc Rev. 2006; 35(6):500–511. [PubMed: 16729144]
17. Terreno E, Dastru W, Delli Castelli D, Gianolio E, Geninatti Crich S, Longo D, Aime S. Advances in metal-based probes for MR molecular imaging applications. Curr Med Chem. 2010; 17(31): 3684–3700. [PubMed: 20846110]
18. Hancu I, Dixon WT, Woods M, Vinogradov E, Sherry AD, Lenkinski RE. CEST and PARACEST MR contrast agents. Acta Radiol. 2010; 51(8):910–923. [PubMed: 20828299]
19. Goffeney N, Bulte JW, Duyn J, Bryant LH Jr. van Zijl PC. Sensitive NMR detection of cationic-polymer-based gene delivery systems using saturation transfer via proton exchange. J Am Chem Soc. 2001; 123(35):8628–8629. [PubMed: 11525684]
20. McMahon MT, Gilad AA, DeLiso MA, Berman SM, Bulte JW, van Zijl PC. New "multicolor" polypeptide diamagnetic chemical exchange saturation transfer (DIACEST) contrast agents for MRI. Magn Reson Med. 2008; 60(4):803–812. [PubMed: 18816830]
21. Zhou J, Payen JF, Wilson DA, Traystman RJ, van Zijl PC. Using the amide proton signals of intracellular proteins and peptides to detect pH effects in MRI. Nat Med. 2003; 9(8):1085–1090. [PubMed: 12872167]
22. Ling W, Regatte RR, Navon G, Jerschow A. Assessment of glycosaminoglycan concentration in vivo by chemical exchange-dependent saturation transfer (gagCEST). Proc Natl Acad Sci U S A. 2008; 105(7):2266–2270. [PubMed: 18268341]
23. van Zijl PC, Jones CK, Ren J, Malloy CR, Sherry AD. MRI detection of glycogen in vivo by using chemical exchange saturation transfer imaging (glycoCEST). Proc Natl Acad Sci U S A. 2007; 104(11):4359–4364. [PubMed: 17360529]
24. Cai K, Haris M, Singh A, Kogan F, Greenberg JH, Hariharan H, Detre JA, Reddy R. Magnetic resonance imaging of glutamate. Nat Med. 2012; 18(2):302–306. [PubMed: 22270722]
25. Li X, Huang W, Morris EA, Tudorica LA, Seshan VE, Rooney WD, Tagge I, Wang Y, Xu J, Springer CS Jr. Dynamic NMR effects in breast cancer dynamic-contrast-enhanced MRI. Proc Natl Acad Sci U S A. 2008; 105(46):17937–17942. [PubMed: 19008355]

26. Yankeelov TE, Lepage M, Chakravarthy A, Broome EE, Niermann KJ, Kelley MC, Meszoely I, Mayer IA, Herman CR, McManus K, Price RR, Gore JC. Integration of quantitative DCE-MRI and ADC mapping to monitor treatment response in human breast cancer: initial results. Magn Reson Imaging. 2007; 25(1):1–13. [PubMed: 17222711]
27. Griffiths JR, McIntyre DJ, Howe FA, Stubbs M. Why are cancers acidic? A carrier-mediated diffusion model for H+ transport in the interstitial fluid. Novartis Found Symp. 2001; 240:46–62. discussion 62-47, 152-153. [PubMed: 11727936]
28. Zhang X, Lin Y, Gillies RJ. Tumor pH and its measurement. J Nucl Med. 2010; 51(8):1167–1170. [PubMed: 20660380]
29. Gatenby RA, Gillies RJ. A microenvironmental model of carcinogenesis. Nat Rev Cancer. 2008; 8(1):56–61. [PubMed: 18059462]
30. Chan, KWY.; McMahon, MT.; Liu, G.; Kato, Y.; Bhujwalla, ZM.; Artemov, D.; van Zijl, PCM. Imaging of glucose uptake in breast tumors using non-labeled D-glucose. Proceedings of the 19th Annual Meeting of ISMRM; 2011; Montreal, Canada.
31. Walker-Samuel, S.; Johnson, P.; Pedley, B.; Lythgoe, MF.; Golay, X. Assessment of tumour glucose uptake using gluco-CEST. Proceedings of the 19th Annual Meeting of ISMRM; 2011; Montreal, Canada.
32. Walker-Samuel, S.; Ramasawmy, R.; Torrealdea, F.; Rega, M.; Johnson, P.; Rajkumar, V.; Richardson, S.; Thomas, D.; Pedley, B.; Golay, X.; Lythgoe, MF. Compartmental modelling of regional tumour glucose pharmacokinetics with quantitative glucoseCEST. Proceedings of the 20th Annual Meeting of ISMRM; 2012; Melbourne, Australia.
33. Walker-Samuel, S.; Ramasawmy, S.; Torrealdea, F.; Rega, M.; Johnson, P.; Rajkumar, V.; Richardson, S.; Thomas, D.; Pedley, B.; Lythgoe, MF.; Golay, X. Quantitative imaging of tumour glucose uptake using glucoseCEST: comparison with 18F-FDG autoradiography. Proceedings of the 20th Annual Meeting of ISMRM; 2012; Melbourne, Australia.
34. Kim M, Gillen J, Landman BA, Zhou J, van Zijl PC. Water saturation shift referencing (WASSR) for chemical exchange saturation transfer (CEST) experiments. Magn Reson Med. 2009; 61(6): 1441–1450. [PubMed: 19358232]
35. Zhu, W.; Kato, Y.; Shankar, S.; Bhujwalla, ZM.; Artemov, D. Assessment of Tumor Microvasculature by a Kinetic Model Independent DCE-MRI Method Using a High Molecular Weight Contrast Agent. Proceedings of the 18th Annual Meeting of ISMRM; 2010; Stockholm, Sweden.
36. Zhou JY, van Zijl PCM. Chemical exchange saturation transfer imaging and spectroscopy. Prog Nucl Mag Res Sp. 2006; 48(2–3):109–136.
37. Zhou J, Wilson DA, Sun PZ, Klaus JA, Van Zijl PC. Quantitative description of proton exchange processes between water and endogenous and exogenous agents for WEX, CEST, and APT experiments. Magn Reson Med. 2004; 51(5):945–952. [PubMed: 15122676]
38. McMahon MT, Gilad AA, Zhou J, Sun PZ, Bulte JW, van Zijl PC. Quantifying exchange rates in chemical exchange saturation transfer agents using the saturation time and saturation power dependencies of the magnetization transfer effect on the magnetic resonance imaging signal (QUEST and QUESP): Ph calibration for poly-L-lysine and a starburst dendrimer. Magn Reson Med. 2006; 55(4):836–847. [PubMed: 16506187]
39. Bhujwalla ZM, Artemov D, Natarajan K, Ackerstaff E, Solaiyappan M. Vascular differences detected by MRI for metastatic versus nonmetastatic breast and prostate cancer xenografts. Neoplasia. 2001; 3(2):143–153. [PubMed: 11420750]
40. Zhou J, Lal B, Wilson DA, Laterra J, van Zijl PC. Amide proton transfer (APT) contrast for imaging of brain tumors. Magn Reson Med. 2003; 50(6):1120–1126. [PubMed: 14648559]
41. Macheda ML, Rogers S, Best JD. Molecular and cellular regulation of glucose transporter (GLUT) proteins in cancer. J Cell Physiol. 2005; 202(3):654–662. [PubMed: 15389572]
42. Grover-McKay M, Walsh SA, Seftor EA, Thomas PA, Hendrix MJ. Role for glucose transporter 1 protein in human breast cancer. Pathology oncology research. 1998; 4(2):115–120. [PubMed: 9654596]
43. Gullino PM, Grantham FH, Courtney AH. Glucose consumption by transplanted tumors in vivo. Cancer Res. 1967; 27(6):1031–1040. [PubMed: 4290857]

44. Hossmann KA, Niebuhr I, Tamura M. Local cerebral blood flow and glucose consumption of rats with experimental gliomas. J Cereb Blood Flow Metab. 1982; 2(1):25–32. [PubMed: 7061601]
45. McLarty K, Moran MD, Scollard DA, Chan C, Sabha N, Mukherjee J, Guha A, McLaurin J, Nitz M, Houle S, Wilson AA, Reilly RM, Vasdev N. Comparisons of [18F]-1-deoxy-1-fluoro-scyllo-inositol with [18F]-FDG for PET imaging of inflammation, breast and brain cancer xenografts in athymic mice. Nucl Med Biol. 2011; 38(7):953–959. [PubMed: 21982567]
46. Montcourrier P, Silver I, Farnoud R, Bird I, Rochefort H. Breast cancer cells have a high capacity to acidify extracellular milieu by a dual mechanism. Clin Exp Metastasis. 1997; 15(4):382–392. [PubMed: 9219726]
47. Schornack PA, Gillies RJ. Contributions of cell metabolism and H+ diffusion to the acidic pH of tumors. Neoplasia. 2003; 5(2):135–145. [PubMed: 12659686]
48. van Zijl PC, Jones CK, Ren J, Malloy CR, Sherry AD. MRI detection of glycogen in vivo by using chemical exchange saturation transfer imaging (glycoCEST). Proc Natl Acad Sci U S A. 2007; 104(11):4359–4364. [PubMed: 17360529]
49. Tourdias T, Rodrigo S, Oppenheim C, Naggara O, Varlet P, Amoussa S, Calmon G, Roux FX, Meder JF. Pulsed arterial spin labeling applications in brain tumors: practical review. Journal of Neuroradiology. 2008; 35(2):79–89.
50. Barrett T, Brechbiel M, Bernardo M, Choyke PL. MRI of tumor angiogenesis. J Magn Reson Imaging. 2007; 26(2):235–249. [PubMed: 17623889]
51. Wolf RL, Detre JA. Clinical neuroimaging using arterial spin-labeled perfusion magnetic resonance Imaging. Neurotherapeutics. 2007; 4(3):346–359. [PubMed: 17599701]
52. Noguchi T, Yoshiura T, Hiwatashi A, Togao O, Yamashita K, Nagao E, Shono T, Mizoguchi M, Nagata S, Sasaki T, Suzuki SO, Iwaki T, Kobayashi K, Mihara F, Honda H. Perfusion imaging of brain tumors using arterial spin-labeling: Correlation with histopathologic vascular density. Am J Neuroradiol. 2008; 29(4):688–693. [PubMed: 18184842]
53. Kim MJ, Kim HS, Kim JH, Cho KG, Kim SY. Diagnostic accuracy and interobserver variability of pulsed arterial spin labeling for glioma grading. Acta Radiol. 2008; 49(4):450–457. [PubMed: 18415790]
54. Warmuth C, Gunther M, Zimmer C. Quantification of blood flow in brain tumors: comparison of arterial spin labeling and dynamic susceptibility-weighted contrast-enhanced MR imaging. Radiology. 2003; 228(2):523–532. [PubMed: 12819338]
55. Kawashima M, Katada Y, Shukuya T, Kojima M, Nozaki M. MR perfusion imaging using the arterial spin labeling technique for breast cancer. J Magn Reson Imaging. 2012; 35(2):436–440. [PubMed: 22095487]
56. Zhu DC, Buonocore MH. Breast tissue differentiation using arterial spin tagging. Magn Reson Med. 2003; 50(5):966–975. [PubMed: 14587007]
57. Pedrosa I, Alsop DC, Rofsky NM. Magnetic Resonance Imaging as a Biomarker in Renal Cell Carcinoma. Cancer. 2009; 115(10):2334–2345. [PubMed: 19402070]
58. Lozner EL, Winkler AW, Taylor FH, Peters JP. The Intravenous Glucose Tolerance Test. The Journal of clinical investigation. 1941; 20(5):507–515. [PubMed: 16694855]
59. Zhou J, Blakeley JO, Hua J, Kim M, Laterra J, Pomper MG, van Zijl PC. Practical data acquisition method for human brain tumor amide proton transfer (APT) imaging. Magn Reson Med. 2008; 60(4):842–849. [PubMed: 18816868]
60. Zhu H, Jones CK, van Zijl PC, Barker PB, Zhou J. Fast 3D chemical exchange saturation transfer (CEST) imaging of the human brain. Magn Reson Med. 2010; 64(3):638–644. [PubMed: 20632402]
61. Jones CK, Polders D, Hua J, Zhu H, Hoogduin HJ, Zhou J, Luijten P, van Zijl PC. In vivo three-dimensional whole-brain pulsed steady-state chemical exchange saturation transfer at 7 T. Magn Reson Med. 2012; 67(6):1579–1589. [PubMed: 22083645]

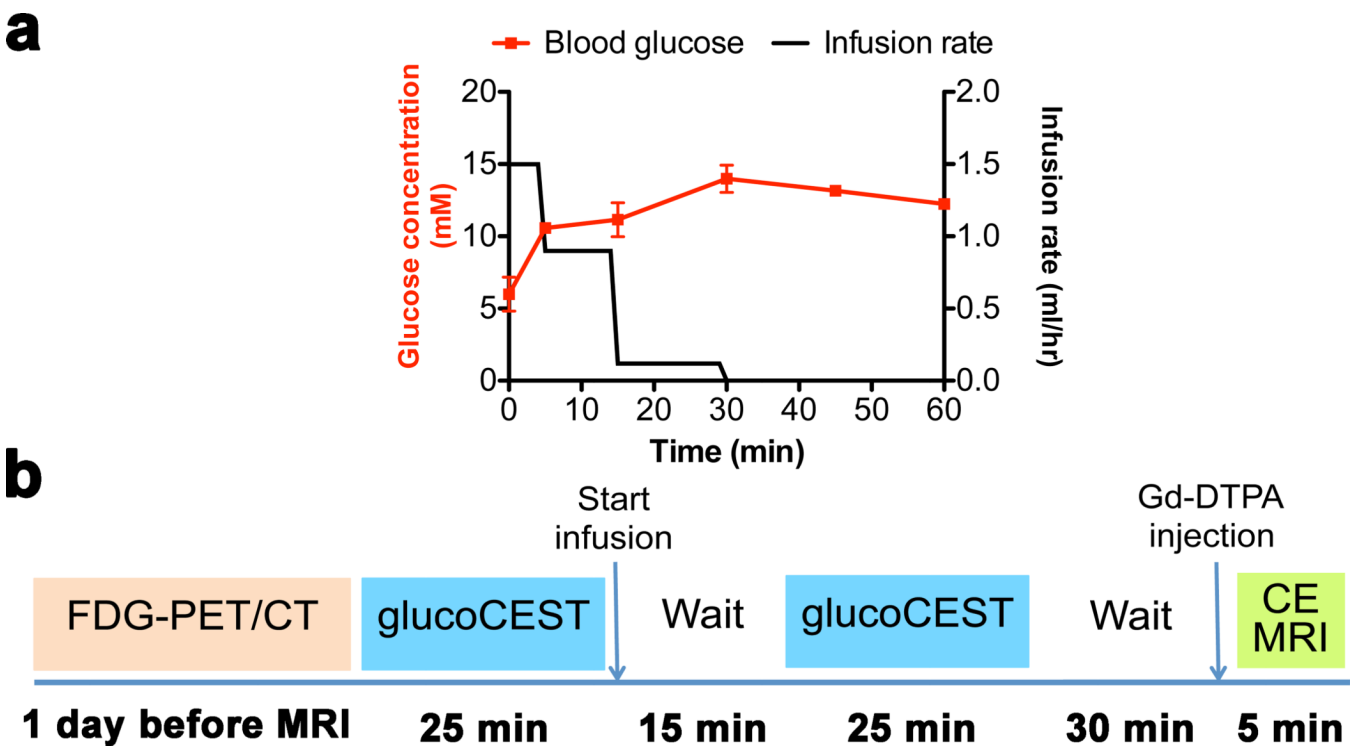

Figure 1. Glucose infusion protocol with blood concentrations measured (a) and MRI protocol (b)

The rate of glucose infusion (black curve) resulted in blood glucose concentrations as shown by the red curve. The blood glucose concentration was measured for two mice (average ± SD). CE: contrast enhanced.

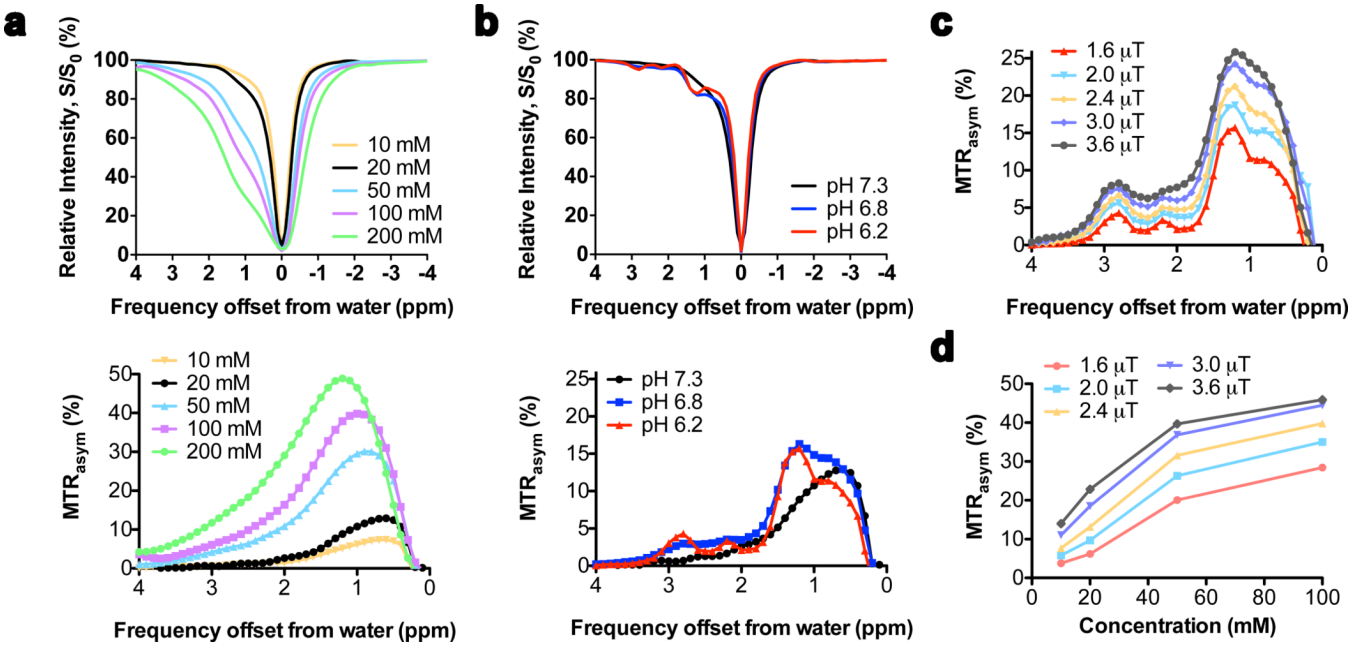

Figure 2. Concentration, pH and radiofrequency (RF) saturation field (B_1) dependence of glucoCEST contrast in D-glucose solutions in PBS at 37°C at 11.7T

(**a**) Z-spectra (top) and MTR_{asym} (bottom) as a function of concentration at pH 7.3 for B_1=1.6 μT; (**b**) Z-spectra (top) and MTR_{asym} (bottom) as a function of pH for 20 mM D-glucose at B1 = 1.6 μT; a slow down of exchange at low pH increases the contrast of several OH protons, especially peaks at 1.2, 2.2 and 2.8 ppm. (**c**) MTR_{asym} spectra as a function of B_1 for 20 mM D-glucose at pH 6.2. (**d**) glucoCEST contrast (averaged MTR_{asym} over 0.8–2.2 ppm) as a function of concentration at different B_1.

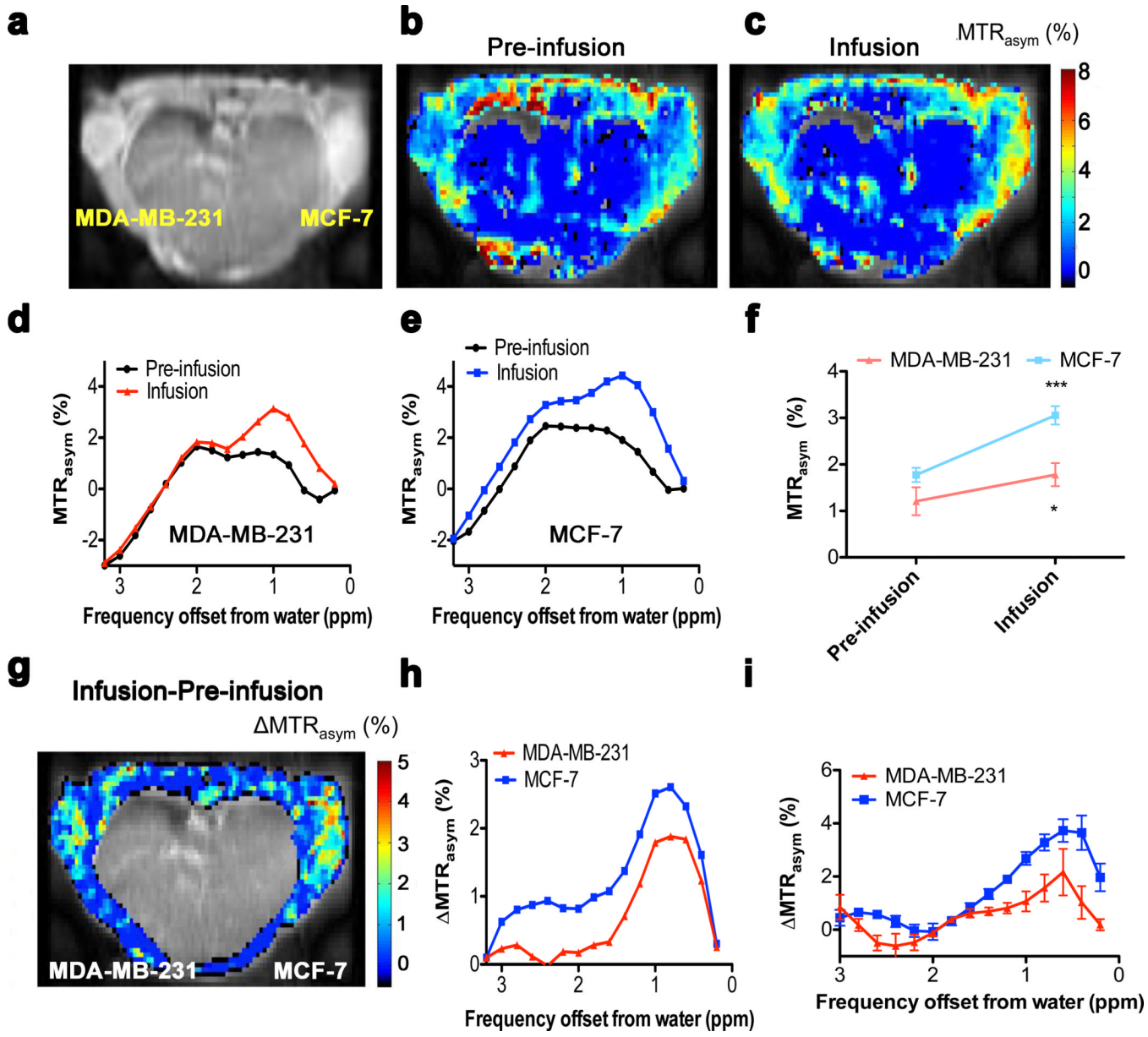

Figure 3. GlucoCEST results for a mouse inoculated with MDA-MB-231 and MCF-7 breast tumors (a–i)

(**a**) Anatomical image for a mouse inoculated with breast tumors. (**b,c**) GlucoCEST images (average MTR_{asym} % over spectral points between 0.8–2.2 ppm) before infusion (**b**) and during infusion (**c**). (**d,e**) Pre-infusion and Infusion MTR_{asym} spectra from ROIs including the whole tumor for MDA-MB-231 (**d**) and MCF-7 (**e**). (**f**) MTR_{asym} values pre-infusion and during infusion (n = 5; * $p < 0.05$; *** $p < 0.005$). (**g**) GlucoCEST difference map: $\Delta MTR_{asym} = MTR_{asym}(\text{Infusion}) - MTR_{asym}(\text{Pre-infusion})$. The intensity of the internal body was thresholded out because it contains moving areas (lungs and heart) that have large magnetic susceptibility differences with surrounding tissues, which complicates difference imaging. The ΔMTR_{asym} profiles (**h**) of MDA-MB-231 and MCF-7 show a profile resembling that of D-glucose in phantoms in Fig. 2. (**i**) Average ΔMTR_{asym} difference spectrum for 5 mice.

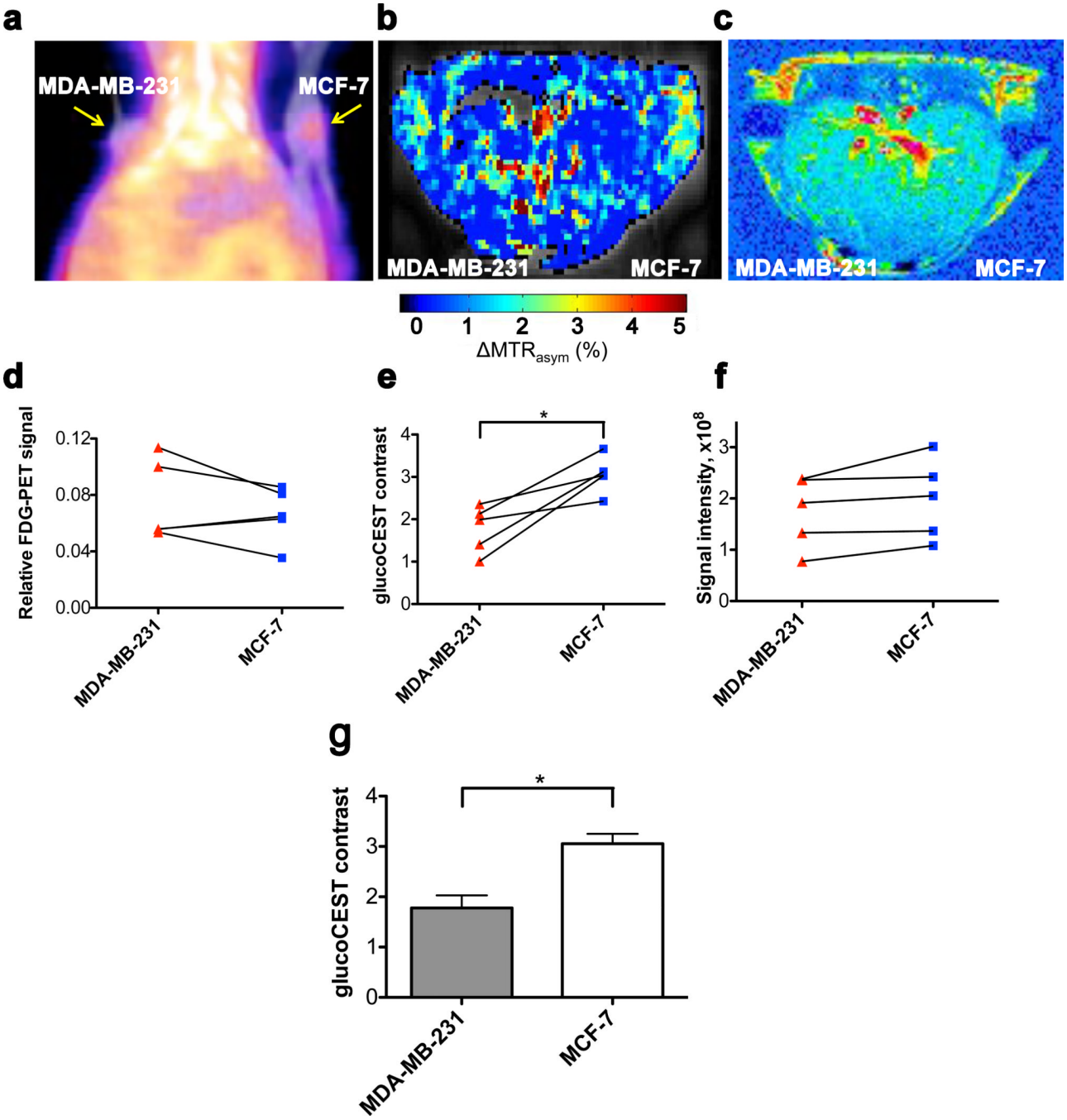

Figure 4. Non-edited ^{18}FDG-PET/CT, glucoCEST and contrast-enhanced (CE) difference images *in vivo*

(**a**) ^{18}FDG-PET/CT coronal view obtained one hour after intravenous (i.v.) injection of ^{18}FDG showing accumulation in both tumors. (**b**) GlucoCEST ΔMTR_{asym} map (Infusion – Pre-infusion). (**c**) T_1-weighted difference image (Injection – pre-injection) showing Gd-enhanced regions, mainly in the edges of tumors. (**d–f**) Comparison of signal intensities (n = 5) for the three modalities using ROIs comprising the two tumors. Even though some trends appear visible for PET and contrast-enhanced MRI, significant differences ($p<0.05$; paired student's t-test) between the tumors could be detected only in glucoCEST. (**g**) Bar graph showing average glucoCEST contrast for MDA-MB-231 and MCF-7 tumors.

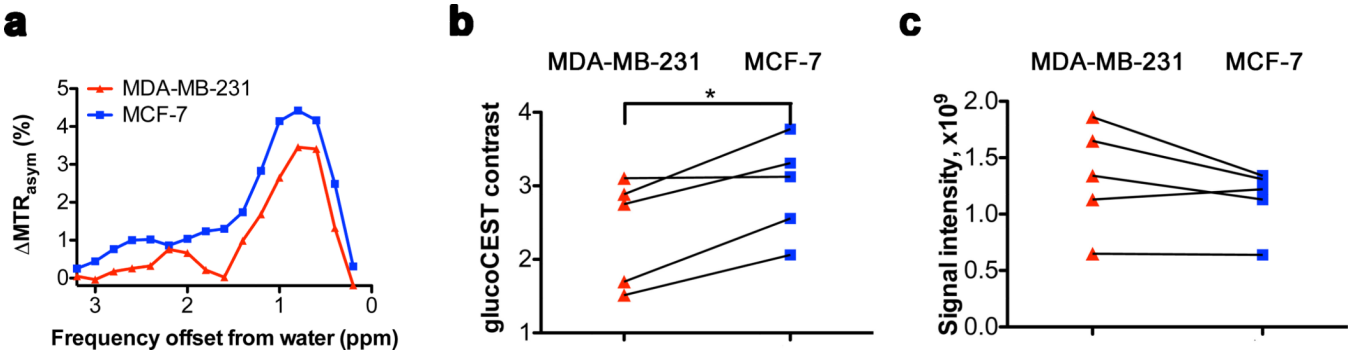

Figure 5. GlucoCEST and CE-MRI data in tumor regions enhanced in MRI perfusion imaging

(**a**) ΔMTR_{asym} spectra for MDA-MB-231 and MCF-7. Note the distinctive glucose shape for the difference profiles. (**b**) Quantitative glucoCEST shows a significant difference (N = 5; $p<0.05$; paired student's t-test) between tumor types (**c**) Quantitative CE-MRI shows no significant difference (N = 5; $p>0.05$; paired student's t-test) between tumor types.

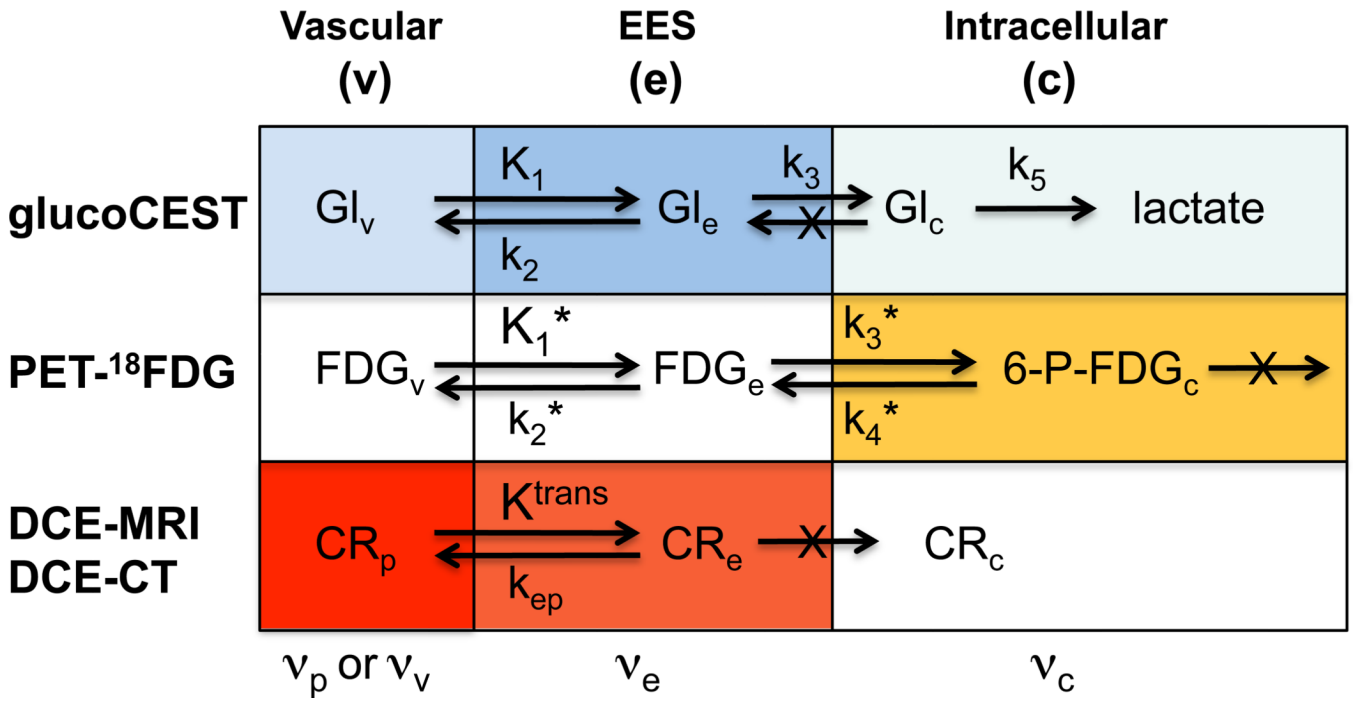

Figure 6. Overview of rate constants and contrast contributions (darker color = higher contrast; white is negligible contrast) for glucoCEST, ^{18}FDG-PET and contrast enhanced MRI and CT in tumors

For glucoCEST, the glucose concentrations in vascular space and EES are comparable, but due to lower pH the EES has higher signal contribution. Intracellular signal is very small to negligible due to rapid glycolysis. In PET, the signal is predominantly due to trapped intracellular phosphorylated FDG. For contrast enhanced MR and CT, the agents occupy only plasma in blood and while they enter the interstitium, the EES concentration is generally lower than in plasma due to limited K^{trans}. Glucose, on the other hand moves freely into the interstitium and the erythrocytes. v = vascular (plasma + erythrocytes), p = plasma.